J. Fluid Mech. (2008), *vol.* 594, *pp.* 1–28.
doi:10.1017/S0022112007008804 Printed in the United Kingdom

Particle-phase distributions of pressure-driven flows of bidisperse suspensions

JAY T. NORMAN, BABATUNDE O. OGUNTADE AND ROGER T. BONNECAZE

Department of Chemical Engineering, The University of Texas at Austin, Austin, TX 78712, USA

(Received 19 February 2006 and in revised form 26 June 2007)

The phase distribution of a bimodal distribution of negatively buoyant particles in a low-Reynolds-number pressure-driven flow of a suspension in a horizontal pipe is measured using multi-frequency electrical impedance tomography (EIT). Suspensions of heavy silver-coated particles and slightly heavy PMMA particles exhibit different effective conductivities depending on the frequency of an applied electrical current. This difference allows the separate imaging of the phase distribution of each particle type and the composite suspension. At low flow rates the dense particles tend to distribute in the lower half of the pipe The particles are resuspended toward the centre as the flow rate is increased. The slightly heavy particles tend to accumulate closer to the centre of the pipe. The presence of the nearly neutrally buoyant particles enhances the resuspension of the heavy particles compared to that of a suspension of heavy particles alone at the same volume fraction. A suspension balance model is used to theoretically predict the distribution of particles in the flow assuming an ideal mixing rule for the particle partial pressures. The agreement between the predictions and the experimental observations is qualitatively correct and quantitatively fair.

1. Introduction

Many suspensions in industrial processes and naturally occurring suspension flows consist of particles with different sizes and densities. A thorough understanding of these suspensions is important in understanding the rheology of such systems and predicting the behaviour of polydisperse suspensions. Here, one type of disperse suspension flow is considered, specifically a low-Reynolds-number pressure-driven pipe flow of a suspension composed of two types of heavy particles with different densities and particle radii.

Considerable research has been devoted to understanding the particle distribution in low-Reynolds-number viscous suspension flows, where inertial effects are negligible. Gadala-Maria & Acrivos (1980) indirectly observed the phenomenon of particle migration in low-Reynolds-number suspension flows from areas of high to low shear in a Couette rheometer. Further, they observed that this migration was a strong function of concentration. They noted a long-term decrease in the viscosity as the suspension was sheared, which they attributed to the migration of particles to the low-shear zone in the reservoir of the rheometer. Studies by Leighton & Acrivos (1987) confirmed this long-term reduction in viscosity and also noted a short-term viscosity increase in the initial shearing of the Couette rheometer. They attributed this short-term increase in viscosity to the migration of particles across the gap of the rheometer. Furthermore, they demonstrated that this phenomenon was shear-induced

particle migration, and they used their studies to evaluate diffusion coefficients, which scaled as the shear rate and the square of the particle radius and were a strong function of concentration.

Numerous experimental studies have focused on the migration of particles of one type in low Reynolds number suspension flows (for example see, Altobelli, Givler & Fukushima 1991; Koh, Hookham & Leal 1994; Hampton *et al.* 1997; Lyon & Leal 1997*a*, *b*; Butler & Bonnecaze 1999; Norman, Nayak & Bonnecaze 2005; and Lenoble, Snabre & Pouligny 2005); however, only a few investigators have focused on viscous suspension with more than one particle type. Beyea, Altobelli & Mondy (2003) used chemically selective nuclear magnetic resonance (NMR) imaging to observe the sedimentation of bidisperse suspensions. Husband *et al.* (1994) used direct visualization with tracer particles to observe particle migration in non-homogeneous Couette and open surface shear flows and found that larger particles migrate faster than smaller particles. Shauly, Wachs & Nir (1998) investigated the effect of particle radii on shear-induced particle migration in a Couette device. They observed a higher concentration of the particles with the largest radii in the low shear rate zone of the flow. Lyon & Leal (1998*b*) investigated a bidisperse (different radii) suspension of neutrally buoyant particles in a pressure-driven channel flow. They used laser-Dopler velocimetry (LDV) to determine the concentration profile of each particle type. Similar to the studies by Shauly *et al.*, they found that the particles segregated with a greater fraction of large particles in the centre of the channel. Further, they observed that this segregation of particle size was more apparent at lower concentrations. Theoretically, Chang & Powell (1993, 1994) used Stokesian dynamics simulations to measure self-diffusion and viscosity of the neutrally buoyant suspensions of bidisperse particles.

Other studies of bidisperse suspensions have focused on systems with particles of differing density. For instance, Tripathi & Acrivos (1998) studied viscous resuspension in a Couette type flow where one type of particle was heavier than the suspending fluid and another particle type was density matched to the suspending fluid. They observed that the initially settled bed of heavier particles were resuspended into the fluid containing the neutrally buoyant particles when a shear was applied to suspension, and that the resuspension height of the particles was greater when neutrally buoyant particles were present. This is due to the increased shear-induced migration from the addition of neutrally buoyant particles. Tripathi & Acrivos also extended the diffusion flux model to predict this resuspension phenomenon.

In this paper bimodal suspensions of particles with two different radii and density are investigated. Specifically, suspensions of dense, silver-coated particles and almost neutrally buoyant PMMA particles at low Reynolds number in pressure-driven pipe flows are studied. Multiple-frequency electrical resistance tomography (ERT) measurements are used to determine the particle distribution of each particle type. In § 2 ERT imaging is discussed, including the mathematical modelling. The frequency response of the particles and the measurement technique used to separate the two particle phases is discussed in § 3. In § 4 the experiment is described in detail, including the experimental configuration and the operating parameters. The suspension balance model for a bimodal suspension is presented in § 5. The pressure distribution is discussed in § 6, including a comparison to the pressure distribution of a single-particle-type suspension at similar experimental conditions. Further, the pressure distribution is related to the fully developed state. The experimental results are discussed § 7, including the bulk particle distribution for the bimodal suspensions and the particle distribution for each particle phase. These results are discussed in detail and compared to particle-phase distributions of the single-particle-type suspension at

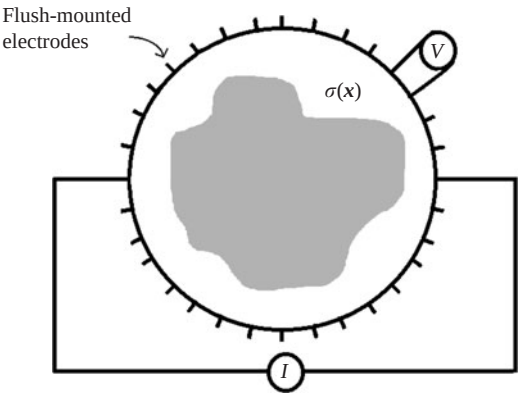

FIGURE 1. Four-electrode (opposite) measuring protocol. Current (I) is injected on flush-mounted opposing electrodes and the resulting potential differences (V) are measured on all adjacent electrodes not used for current injection. The current pair is shifted to the next pair of electrodes and potential measurements are obtained on the remaining electrodes. This procedure is repeated until all possible independent measurements are obtained.

similar experimental conditions. Further, the suspension balance model introduced by Nott & Brady (1994) is extended to this bimodal suspension and compared to the experimental results. The paper concludes with brief remarks.

2. Electrical resistance tomography imaging

The opacity of suspension flows often makes it difficult to determine the particle distribution. However, several methods have been used to non-invasively image particle migration in low-Reynolds-number suspension flows. For example, Phillips *et al.* (1992) used nuclear magnetic resonance imaging (NMRI) to determine concentration fields in suspensions of neutrally buoyant particles sheared in a Couette device. Chow *et al.* (1994), Hampton *et al.* (1997) and Butler, Majors & Bonnecaze (1999) also used NMRI in their studies of low Reynolds number suspension flows. Another imaging technique used by investigators was laser-Doppler velocimetry (LDV), which requires matching of index of refraction. Lyon & Leal (1997*a*, *b*) used this method in several studies to determine concentration fields of neutrally buoyant particles in pressure-driven channel flows. More recently, Butler & Bonnecaze (1999), Norman *et al.* (2005) and Norman & Bonnecaze (2005) investigated particle migration in pressure-driven pipe flow using electrical resistance tomography (ERT).

2.1. *ERT measurements*

ERT imaging is based on the variation in potential fields due to the applied current through a material with varying impedance. A potential field, which is determined by the conductivity distribution in the imaging plane, is produced by introducing a current through a series of electrodes surrounding the plane of interest. The resulting potentials are measured at the electrodes surrounding the image plane. A nonlinear inverse algorithm is used to convert these potential measurements into the previously unknown conductivity field, and these computed conductivity profiles are transformed to concentration fields of the multiphase flows using established correlations. Figure 1 shows a common four-electrode measurement configuration for ERT imaging.

In this study all of the data are obtained with the Mark 2 (Mk.2) EIT data acquisition system (Etuke 1994), which operates at frequency ranging from 1 to 300 kHz. The Mk.2 can perform either current injection with a range of 0–25 mA or potential injection at range of 0 – 5 V. Additionally, the Mk.2 can be programmed with several measurement protocols such as the opposite protocol shown in figure 1 (see Norman *et al.* 2005 for further information).

2.2. *Image reconstruction*

The solution of a nonlinear inverse problem is used to obtain the previously unknown conductivity profile. The inverse method used in this study is the minimization of L_2 norms, which alone results in an ill-conditioned matrix (Parker 1994); therefore, a regularization technique is incorporated to address these problems. The mathematical statement of this regularized nonlinear inverse problem is

$$\min 2\chi(\sigma) = ||\boldsymbol{W}_d \cdot (\boldsymbol{d}^{obs} - \boldsymbol{d}^{calc})||_2^2 + \lambda ||\boldsymbol{W}_m \cdot (\sigma - \sigma_r)||_2^2. \tag{2.1}$$

Here, the first L_2 norm in (2.1) represents the squared difference in the noisy, measured data $\boldsymbol{d}^{obs}$, and the calculated potentials $\boldsymbol{d}^{calc}$. The calculated potential is determined with a pseudo three-dimensional finite element (FE) program (see Norman 2004 for further information on the forward and inverse modelling). The parameter $\boldsymbol{W}_d$ is the data-weighting matrix, which is a diagonal matrix of the inverse of the squared potential measurements. The second L_2 norm represents the regularization of the inversion. Regularization ensures a sufficiently smooth solution of the conductivity σ relative to some reference conductivity σ_r. In this study, the model-weighting matrix $\boldsymbol{W}_m$ is the difference matrix (a simple representation of the first derivative), which results in the smoothest solution with respect to the reference conductivity. The parameter λ is a positive, numerically determined coefficient optimized at each iteration.

Minimization of (2.1) results in an equation for the update in the conductivity profile. A numerical algorithm is implemented to determine the conductivity profile with the smallest L_2 error. This inverse algorithm was verified by reconstructing synthetically produced potential measurements with different levels of random noise (see Norman 2004 for further information).

In this study a 32-electrode opposite measurement protocol was used to perform all measurements. This technique produces 448 independent measurements; however, the symmetry of the system studied here reduces that number to 224 independent measurements. In this study, a maximum of 128 elements were used in the inverse problem, and each element represents a constant-conductivity zone and, therefore, one independent measurement.

3. Frequency response of particles in an ionic solution

Suspensions of conductive particles, such as the silver-coated spheres (hereafter referred to as Ag spheres) suspended in ionic solutions used in this study, respond to injected current differently at different frequencies. Etuke (1994) exploited this property to differentiate between nickel (Ni) and glass particles suspended in a sodium chloride (NaCl) solution. By injecting current and measuring the resulting potential field, it was determined that a suspension of Ni particles displayed a critical frequency at which the suspension had the same conductivity as the suspending fluid. Further, it was observed that below the critical frequency, the Ni particles actually depressed the conductivity of the suspension. Using just the real portion of the

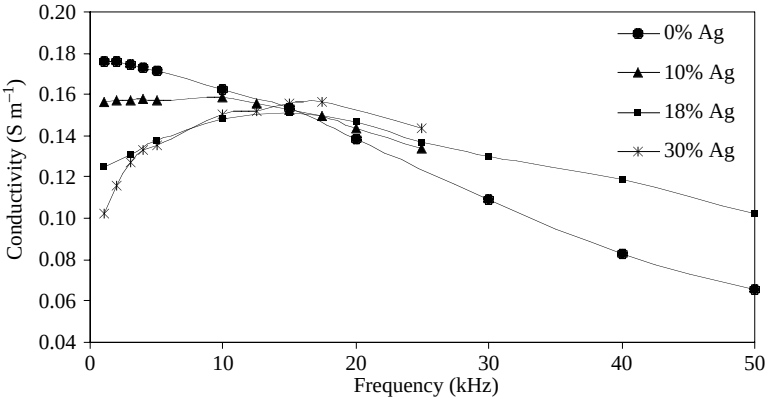

FIGURE 2. Frequency response of uniformly distributed silver particles in a suspending fluid with a conductivity of 0.176 S m^{-1} at zero frequency.

potential measurements, a correlation for the volume fraction of each particle type (Ni and glass) as a function of the overall conductivity at a specified frequency was produced. Here the frequency response of conducting particles in an ionic solution is exploited to determine the phase distribution of a suspension of heavy, silver (Ag) particles and heavy, non-conducting poly-methyl methacrylate (PMMA) particles in a low-Reynolds-number pressure-driven pipe flow.

Preliminary experiments were performed to determine the frequency response of the Ag particles as a function of the ionic strength of the suspending fluid. The conductivity of the suspending fluid was controlled by the addition of an aqueous solution of sodium iodide (NaI) to a viscous fluid (UCON® 75-H-90000 obtained from the Dow Chemical Company). At a very low concentration of NaI, the Ag particles always increased the conductivity of the suspending fluid in proportion to the volume fraction of particles added. As the ionic concentration of the suspending fluid was increased, the addition of Ag particles depressed the conductivity of the suspending fluid at low frequencies. However, at some critical frequency the conductivity of the suspension of Ag particles and the suspending fluid are the same, and after this point it appears that the conductivity of the suspension is greater than the conductivity of the suspending fluid. In order to obtain the desired density range for the experiments in this study (which increases with increasing ionic concentration) a suspending fluid of 1760 μS cm^{-1} was mixed and tested. Figure 2 displays the frequency response of this suspending fluid with various concentrations of Ag particles uniformly distributed in the pipe.

Figure 2 reveals that the critical frequency occurs at approximately 15 kHz, and that the critical frequency is independent of the concentration of Ag particles suspended in the fluid. To distinguish the two particle phases, the frequency dependence of the PMMA particles in the same suspending fluid must also be known. Figure 3 depicts the frequency response of the PMMA particles at various concentrations in the same suspending fluid.

Clearly, from figure 3, the PMMA particles do not exhibit the same frequency dependence as the Ag particles; their addition depresses the conductivity throughout the frequency range used in this study. Further, this figure indicates a relatively constant reduction in the suspension conductivity at a frequency range that is used for

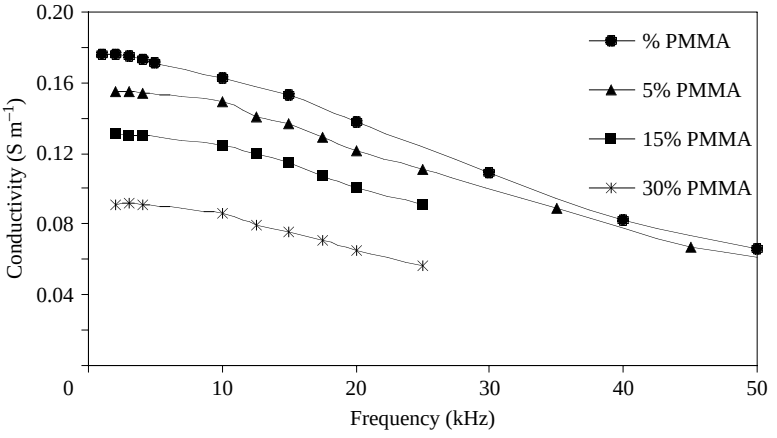

FIGURE 3. Frequency response of the non-conducting PMMA particles in a suspending fluid with a conductivity of $0.176\,\mathrm{S\,m^{-1}}$ at zero frequency.

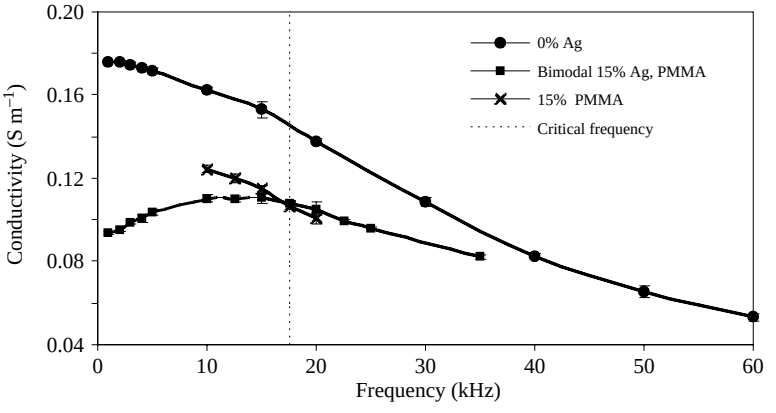

FIGURE 4. Typical frequency response of in a $0.176\,\mathrm{S\,m^{-1}}$ suspending fluid, a uniformly distributed suspension of 15 % by volume PMMA and a uniformly distributed bimodal suspension of Ag and PMMA particles at 15 % by volume. The vertical dashed line shows the critical frequency at which the silver suspension is transparent.

the bimodal experiments. Most importantly the PMMA particles show a clear trend of reducing the conductivity at the critical frequency of the Ag particle suspension.

To confirm that the particles behave as expected when both types of particles are present in the suspension, a mixture consisting of 70 % by volume of the suspending fluid with a conductivity of $0.176\,\mathrm{S\,m^{-1}}$ and 15 % by volume of each type of particle was mixed to produce a uniform suspension. The frequency response of this bimodal suspension was then measured throughout a range of frequencies, taking care to observe the behaviour of the suspension in the range nearest the critical frequency. Figure 4 shows the response of the bimodal system at varying frequencies, revealing that the bimodal suspension follows the same trends observed for the monomodal systems. Specifically, this figure indicates that at the critical frequency, the system behaves as if it were composed of only PMMA particles. Further, the graph indicates that the critical frequency occurs at 17.5 kHz, which is just below the limit of the sensor array performance.

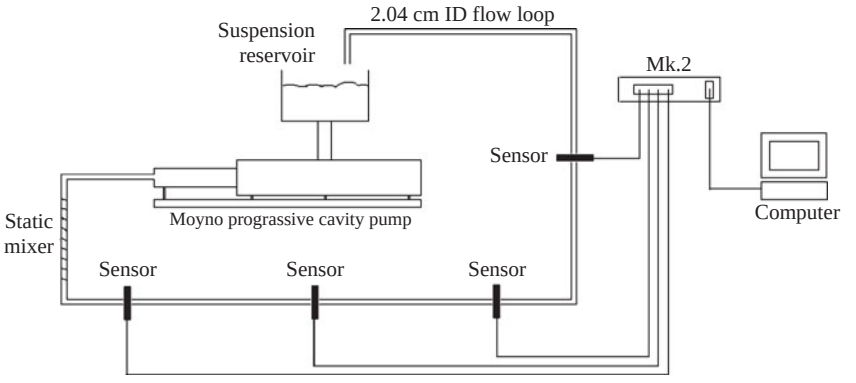

FIGURE 5. Schematic of the flow loop used for the experiments. A Moyno progressing cavity pump is used to create a pressure-driven flow through a 2.04 cm ID pipe. A static mixer just downstream of the pump exit ensures an initially uniform distribution of the particles. Four sensors are shown, along with the Mk.2 system for measurement and a computer interface for data acquisition and manipulation. The total length of the flow loop is approximately 17 m.

The information from these preliminary experiments indicates that the particle distribution of the Ag and PMMA phases can be determined by measuring potential distribution at two different frequencies. The methodology is as follows. The current-injection 32-electrode opposite measurement technique is used to obtain potential measurements at both 1 kHz and 17.5 kHz. At a frequency of 1 kHz the conductivity field represents the combined concentration profile, which will give insight into the behaviour of suspensions when two different particle types interact. The inverted potential measurement at 17.5 kHz results in the conductivity profile for the PMMA particles. Since the electrical properties and conductivity of a bimodal suspension are known, the concentration profile of the Ag particles can be determined from the conductivities obtained at the two frequencies. The following sections describe the experimental conditions and the methods used to determine the concentration profiles, along with an analysis of the experiments.

4. Experimental procedure

To measure the effects of two particle types in a suspension at low Reynolds number in a pressure-driven pipe flow, a suspension consisting of Ag particles and PMMA particles (in equivalent volumes) was mixed and pumped through the flow system depicted in figure 5.

The suspending fluid consisted of a highly viscous fluid UCON® 75-H-90000 and an aqueous solution of sodium iodide. The two particles were added to the suspending fluid to produce a suspension composed of 15 % by volume Ag and 15 % by volume of PMMA particles. The flow system was equipped with four inline sensors arrays. Before adding the mixture to the flow system, the suspension was placed under vacuum to remove any entrained air from the mixing procedure. The suspension was then poured into the flow system reservoir, where it enters the Moyno progressing cavity pump. The suspension was pumped through clear PVC pipes at constant flow rates. A static inline mixer was inserted near the entrance of the flow loop to ensure an initially uniform distribution of the suspension. The pressure was measured at several positions downstream of the inline mixer using an Ashcroft test gauge. These pressure measurements were used to determine the pressure distribution in the flowing

Particles properties	a (cm)	ρ_p (g cm^{-3})	ϕ
Sliver-coated (Ag) spheres			
Conduct-O-Fil®			
S3000-S	0.003	2.50	0.15
PMMA			
Elvacite® 2401	0.018	1.19	0.15

TABLE 1. Suspension composition: the average radii of the particles a, the density of the particles ρ_p and the volume fraction of particles in the suspension ϕ.

Experiment	Q (cm^3 s^{-1})	G (g cm^{-2} s^{-2})	Re_{pipe}	N_b (ρ_{PMMA})	N_b (ρ_{Ag})
1	4.02	331	0.14	1.87	26.4
2	5.46	336	0.19	1.38	19.5
3	9.83	1307	0.34	0.77	10.8

TABLE 2. Summary of the experimental conditions: the average volumetric flow rate is given by Q, the pressure gradient G measured at the end of the pipeline, the pipe-Reynolds number Re_{pipe}, and the buoyancy number given in terms of the average axial velocity (U).

suspension. The Mk.2 was used to measure the potential distribution at each of the four inline sensor arrays.

4.1. *Suspension preparation*

The suspending fluid was prepared by mixing UCON® lubricant 75-H-90000 with an aqueous NaI solution. The NaI solution was added in the appropriate concentration and quantity to produce the desired viscosity, density and conductivity of the suspending fluid. The density was measured with an ERTCO hydrometer, and a Cannon-Fenske viscometer was used to measure the viscosity. These measurements were conducted at room temperature and repeated numerous times to ensure accuracy. The particles were slowly added to the suspending fluid under vigorous stirring to ensure a well-mixed system. This procedure resulted in the entrainment of air; therefore, the suspension was placed under vacuum with constant stirring for a minimum of six hours. To achieve an initially uniform distribution, the particles were resuspended by mixing at very low speeds to ensure no air entrainment. Table 1 summarizes the composition.

The suspending fluid was an approximately 50 % by volume of UCON® lubricant with the remaining fluid an aqueous solution of 37 mg of NaI per cm^3 of distilled water. This resulted in a suspending fluid that had a measured density of 1.09 g cm^{-3}, a viscosity of 983 cP and a uniform conductivity of 0.176 S m^{-1}. The conductivity of the suspending fluid was measured using Corning CheckMate 90 meter. The particles were silver coated, glass spheres (Conduct-O-Fil® S-3000S, by Potter's Industries) with a radius of approximately 0.003 cm and PMMA particles sieved to an average radius of 0.018 cm (Elvacite® 2401, by INEOS Acrylics).

4.2. *Experimental conditions*

Table 2 summarizes the volumetric flow rate, Q, the measured pressure gradient at the end of the flow system, G, the pipe Reynolds number and the experimental buoyancy number for each particle type (Ag and PMMA). The buoyancy number is a measure of the ratio of the buoyancy forces to the viscous forces. For a pressure-driven

suspension flow in a pipe, this may be expressed in terms of the average suspension velocity as

$$N_b = \frac{2(\rho_p - \rho_f)gR^2}{9\eta U}, \tag{4.1}$$

where ρ_p is the density of the particles, ρ_f is the density of the fluid, g is the acceleration due to gravity, R is the radius of the pipe, η is the kinematic viscosity and U is the average axial velocity.

Three different volumetric flow rates were established for the bimodal suspension, and these correspond to the buoyancy numbers presented in table 2, where $N_b(\rho_{PMMA})$ is the buoyancy number based on the average axial velocity and the density of the PMMA particles and $N_b(\rho_{Ag})$ is the buoyancy number based on the average axial velocity and the density of the Ag particles. The volumetric flow rates were determined by averaging several measurements made with a graduated cylinder and a stopwatch and are also displayed in table 2 along with the corresponding pipe Reynolds numbers. The gauge pressure was measured at several points along the flow system for each experiment using an Ashcroft test gauge with increments of 0.1 psi. The pressure gradient, which was determined from the last two pressure measurements along the flow system, is displayed in table 2. The measured pressure and pressure gradients are discussed in detail in § 6.

4.3. *Experimental measurements*

The Mk.2 was used to obtain potential measurements at various predetermined lengths along the flow loop illustrated in figure 5. The sensor arrays were placed at four specific lengths: 5.50 m, 9.98 m, 11.36 m and 13.01 m after the inline mixer. After the Moyno pump was set to the desired volumetric flow rate, the suspensions were allowed to flow until a steady volumetric flow and pressure distribution were measured. The Mk.2 system was attached to each sensor via 32 gold-plated connectors. The electrodes are connected to the Mk.2 in a way that ensures the position of the first measurement is known, which is important since the inverse algorithm requires the first electrode position to be defined. At each of these positions, two measurements were taken with the Mk.2. The first measurements were obtained at a frequency of 1 kHz, which resulted in potentials that were used to determine the bulk conductivity profile. The second measurements were taken at 17.5 kHz (the predetermined critical frequency), which resulted in potential measurements that were used to determine the PMMA conductivity profile. All of these measurements were repeated several times to ensure the precision of the collected potential measurements.

5. Suspension balance model

The suspension balance model incorporates averaged equations for the suspension phase and the particle phases (Nott & Brady 1994; Lenoble *et al.* 2005; Miller & Morris 2006). Norman *et al.* (2005) successfully applied the suspension balance model to determine the particle distribution of single-particle-type suspensions in pressure-driven suspension flows. When more than one particle type is present in the suspension, additional momentum and continuity equations are required to describe all particle phases. Furthermore, the hindered settling function and the viscosity functions must incorporate the effect of the additional particle phases. The study by Altobelli & Mondy (2002) has shown that the hindered settling function for a bimodal suspension

is adequately expressed by

$$f(\phi) = (1-\phi)^{4.4}, \tag{5.1}$$

where $\phi = \phi_1 + \phi_2$ is the total volume fraction, ϕ_1 and ϕ_2 being the concentration of particles of type 1 and 2 respectively. Storms, Ramaro & Weiland (1990) performed experimental studies and found that the relative viscosity of a bimodal suspension is given by

$$\eta_s = \left[1 + \left(\frac{\alpha\phi}{1-\phi/\phi_m}\right)\right]^{3.3\phi_m}. \tag{5.2}$$

The parameter α is a function of the ratio of particle sizes and the volume fraction of the smallest radii particle. The parameter ϕ_m is maximum packing, which is dependent on the size of the particles in the suspension. For the bimodal suspension investigated here, the best values for these parameter are $\alpha = 0.92$ and $\phi_m = 0.74$ (Storms *et al.* 1990). Shapiro & Probstein (1992) have proposed a similar form for the viscosity of a bimodal suspension.

5.1. *Suspension balance model*

The suspension balance model is developed here for a bimodal suspension. The model is expressed so that recirculation in the cross-section and the phase slip are explicitly calculated. The particle equations are presented where index 1 indicates the PMMA particle phase and 2 indicates the Ag particle phase.

The non-dimensional fully developed steady-state continuity equation for the ith particle phase is given by

$$\nabla\cdot(\phi_i\langle\boldsymbol{u}\rangle_i) = 0. \tag{5.3}$$

The corresponding momentum equation for the ith particle phase is given by

$$-\nabla\Pi_i - \frac{9\phi}{2f(\phi)}\left(\frac{R}{a_i}\right)^2(\langle\boldsymbol{u}\rangle_{p_i} - \langle\boldsymbol{u}\rangle) + 2\nabla\cdot\eta_p\langle\boldsymbol{e}\rangle + (\hat{N}_b\phi)_i\boldsymbol{e}_y = 0, \tag{5.4}$$

where the particle pressure Π_i of species i is assumed to follow the ideal mixing relationship

$$\Pi_i = \eta_n\dot{\gamma}\sum_i\left(\frac{\phi_i}{\phi}\right), \tag{5.5}$$

with η_n the normal viscosity given in terms of the suspension viscosity as

$$\eta_n = \left(\frac{\phi}{\phi_m}\right)^2 K_n\eta_s. \tag{5.6}$$

Here we are assuming that the particle pressure is isotropic due to the generally unidirectional nature of the flow. The parameter K_n is a constant parameter, which was chosen as 0.75 for this study. The suspension viscosity η_s is given in (5.2). Further, the buoyancy number for the respective particle phases is given by

$$(\hat{N}_b\phi)_i = \frac{(\rho_i - \rho_f)g}{G}\phi_i. \tag{5.7}$$

In the above equations, $\dot{\gamma}$ is the shear rate, ϕ_i is the volume fraction of the respective particles and $\eta_{pi} = (\eta_s - 1)(\phi_i/\phi)$. The parameter ϕ_m is the maximum packing value of the particles (0.74). The buoyancy number, $\hat{N}_b$, is related to the buoyancy number in table 2 by $\hat{N}_b = (9\eta U/2GR^2)N_b$.

The non-dimensional suspension equations require further explanation. In tensor form, the fully developed steady-state momentum equation is given by

$$\langle \boldsymbol{b} \rangle + \nabla \cdot \langle \boldsymbol{\Sigma} \rangle = 0, \tag{5.8}$$

where $\langle \boldsymbol{b} \rangle$ is the buoyancy force per unit volume and $\langle \Sigma \rangle$ is the total stress of the suspension. The buoyancy force for the suspension is that due to the density difference between each particle type and the suspending fluid density. Therefore, the total buoyancy force is

$$\langle \boldsymbol{b} \rangle = (\rho_1 - \rho_f)\boldsymbol{g}\phi_1 + (\rho_2 - \rho_f)\boldsymbol{g}\phi_2. \tag{5.9}$$

The total stress on the system is the stress due to the fluid and the stress due to the particles, and is given by

$$\langle \boldsymbol{\Sigma} \rangle = -P\boldsymbol{I} + 2\eta\langle \boldsymbol{e} \rangle + \langle \boldsymbol{\Sigma} \rangle_1 + \langle \boldsymbol{\Sigma} \rangle_2 \tag{5.10}$$

where the stress attributed to the particle phases is given by,

$$\langle \boldsymbol{\Sigma} \rangle_1 + \langle \boldsymbol{\Sigma} \rangle_2 = -\Pi\boldsymbol{I} + 2\eta\eta_p\langle \boldsymbol{e} \rangle. \tag{5.11}$$

Using the relationship of η_p to η_s the total suspension stress is

$$\langle \boldsymbol{\Sigma} \rangle = -(P + \Pi)\boldsymbol{I} + 2\eta\eta_s\langle \boldsymbol{e} \rangle. \tag{5.12}$$

Using these relationships, the non-dimensional fully developed steady-state suspension equations are now formulated. The continuity equation for the suspension is

$$\nabla \cdot \langle \boldsymbol{u} \rangle = 0. \tag{5.13}$$

The momentum equation for the suspension is

$$-\nabla P - \nabla\Pi + 2\nabla \cdot \eta_s\langle \boldsymbol{e} \rangle + (\hat{N}_b\phi)_1\boldsymbol{e}_y + (\hat{N}_b\phi)_2\boldsymbol{e}_y = 0. \tag{5.14}$$

Here ϕ is the volume fraction of particles, η_s is the suspension viscosity given by (5.2). The parameter Π is the particle pressure (given in (5.5)) and P is the pressure, which are non-diminsionalized by GR where $G = -\partial P/\partial y$ and R is the pipe radius. Further, $\boldsymbol{u}$ is the velocity of the suspension phase, which was non-dimensionalized by GR^2/η, x was scaled by the radius of the pipe R and the buoyancy number is $\hat{N}_b = (\rho_p - \rho_f)g/G$. Also, $\langle \boldsymbol{e} \rangle$ is the bulk rate of strain. For the bimodal suspension $\phi = (\phi_1 + \phi_2)$ and $\phi_m = 0.74$. The shear rate is given in terms of the bulk rate of strain as

$$\dot{\gamma} = [\langle \boldsymbol{e} \rangle : \langle \boldsymbol{e} \rangle]^{1/2}. \tag{5.15}$$

5.2. *Numerical considerations*

The nonlinearity of the hindrance and effective viscosity functions makes the set of equations given above very difficult to solve. It is solved by the artificial compressibility method (Chorin 1967) which assumes the suspension to be slightly compressible with a modification made to the suspension continuity equation by the addition of an artificial time derivative of pressure. Equation (5.13) is thus replaced by

$$\frac{1}{c^2}\frac{\partial p}{\partial t} = \frac{\partial u}{\partial x} + \frac{\partial v}{\partial y} \tag{5.16}$$

where c is an artificial compressibility term. The transient solution of the modified system has no physical meaning but the steady-state solution satisfies the steady-state

equations to high degree of accuracy. Using this approach, a value is chosen for c and the problem solved until the left-hand side of the modified equation vanishes, (Chorin 1967). Essentially, pressure ceases to be a primary field variable and reduces computational requirements, especially with the planned extension of the numerical analysis to fully three-dimensional suspension flow.

The commercial finite element package FEMLAB was used to solve the above system of equations. The time-dependent solver implements the method-of-lines algorithm and the iterative solver is deemed to have converged when the global error is less than or equal to 10^{-6}. The computational domain is a circle with a non-dimensional radius of one. The mesh is composed of 316 Lagrange quadratic elements with 5320 degrees of freedom.

5.3. *Numerical results*

Figure 6 is representative of the type of results obtained by solving the suspension balance equations, specifically at the intermediate flow rate of $Q = 5.46\,\mathrm{cm^3\,s^{-1}}$ for the bimodal suspension. Figure 6(a) shows the concentration profile for the PMMA particle phase while figure 6(b) depicts the corresponding profile for the Ag particle phase. The combined particle concentration profile is captured by figure 6(c). The axial velocity distribution for a fully developed steady-state flow is shown in figure 6(d). Though pressure was treated as a dependent variable, the pressure profile obtained, represented by figure 6(e), compares well with the profile obtained for the monodisperse case by Norman *et al.* (2005). The vector plot figure 6(f) represents the in-plane velocities, which were found to be very weak and are four orders of magnitude smaller than the axial velocity.

Figures 6(a) and 6(b) clearly show that buoyancy forces affect the distribution of PMMA and Ag particles respectively, with the particles accumulating at the bottom of the pipe. However, the effect of these buoyancy forces on the lighter particle phase (PMMA) is less significant because of the associated low buoyancy number. The combined concentration distribution profile for both particle phases, figure 6(c) shows the same trend. The axial velocity profile distribution, figure 6(d), sheds light on the effect of particle concentration on the velocity distribution. The maximum velocity occurs as expected in the region where the total concentration of particle and hence suspension viscosity are minimal, i.e. above of the centre of the pipe. The computed pressure distribution profile, figure 6(e) shows the cross-sectional variation of this parameter. The vector representation of the in-plane velocities, figure 6(f) show a recirculation pattern (though weak) which is responsible for the qualitative and quantitative trend in the concentration distributions; these were absent when the numerical solutions were performed without considering the in-plane velocities.

6. Pressure distribution and fully developed length

Norman *et al.* (2005) showed that the measurement of the pressure along the flow system gives important insight into the development of the suspension flow and can be used as an indicator of fully developed flow. Figure 7 shows the gauge pressure (kPa) at various positions in the flow loop downstream of the inline mixer.

The pressure gradient ($\mathrm{kPa\,m^{-1}}$) was calculated from the data presented in figure 7 using a second-order finite differencing and is shown in figure 8. The pressure gradients show similar trends to those observed by Norman *et al.* (2005) for monomodal suspensions in a pressure-driven flow. Their study includes a detailed discussion of the behaviour of the pressure gradient.

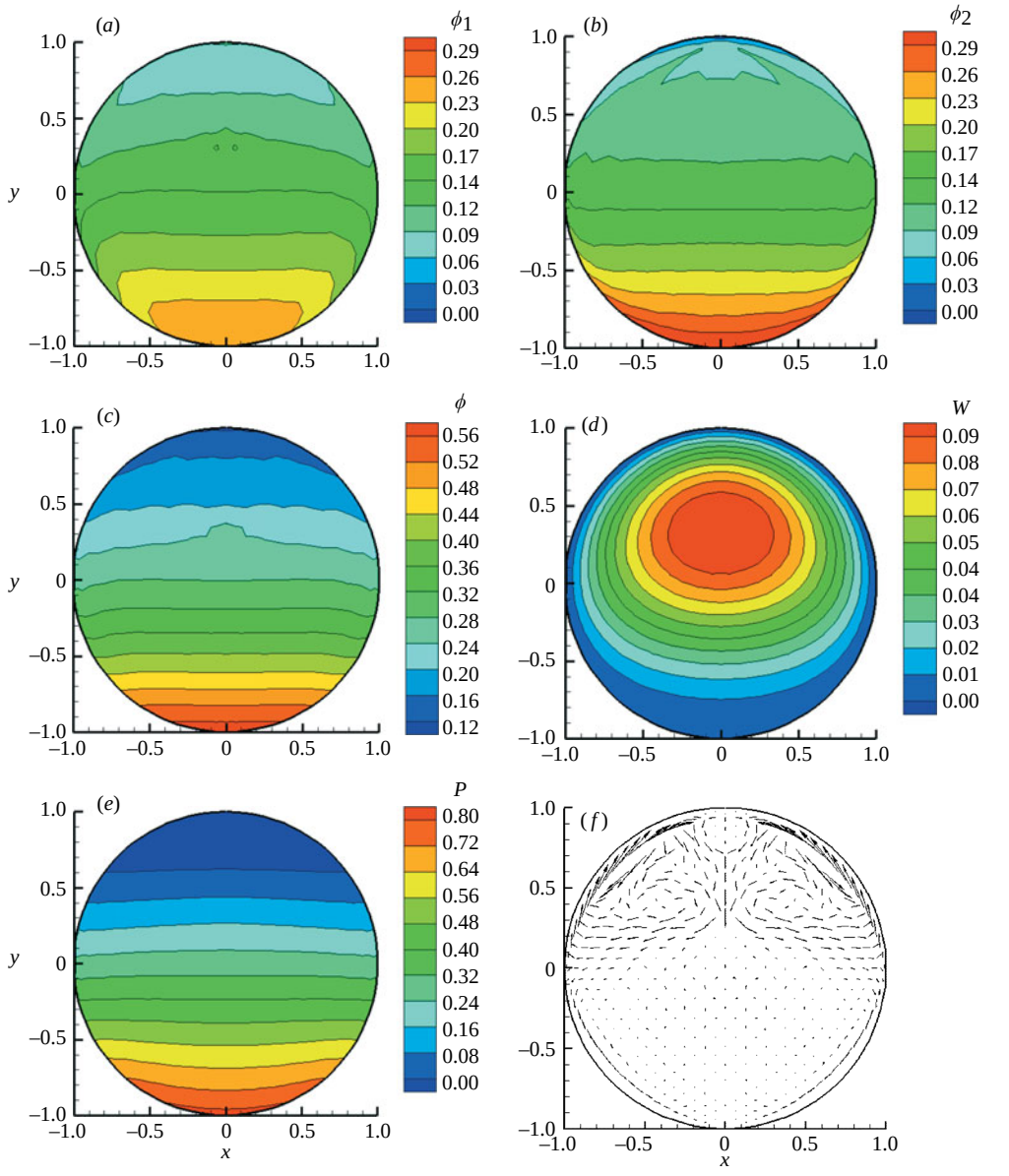

FIGURE 6. Numerical solution of the isotropic suspension balance equations. These results represent a suspension of particles with the properties represented in table 2 for $Q = 5.46\,\mathrm{cm}^3\,\mathrm{s}^{-1}$. (*a*) Volume fraction of PMMA distribution; (*b*) volume fraction of Ag distribution; (*c*) volume fraction of PMMA and Ag distribution; (*d*) non-dimensional axial velocity distribution; (*e*) non-dimensional pressure distribution; (*f*) vector representation of the in-plane velocity distribution.

As seen in figure 8, the pressure gradient reduces to a minimum for the lower flow rates before rising towards the fully developed pressure gradient. As discussed by Norman *et al.*, the developing pressure gradient is an indicator of the progress towards the fully developed state. In this bimodal suspension the lowest flow rate

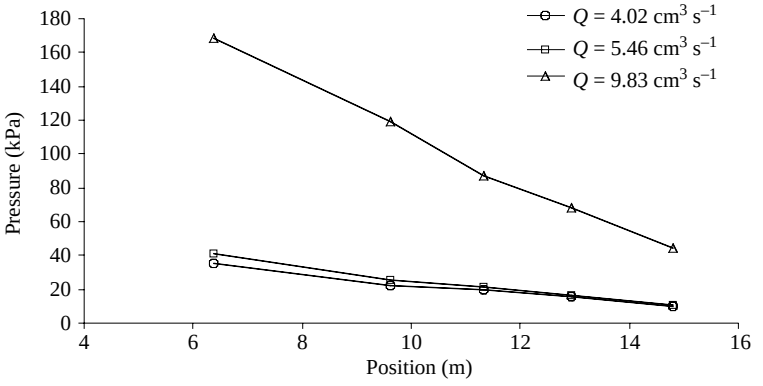

FIGURE 7. Pressure measurements downstream of the static inline mixer.

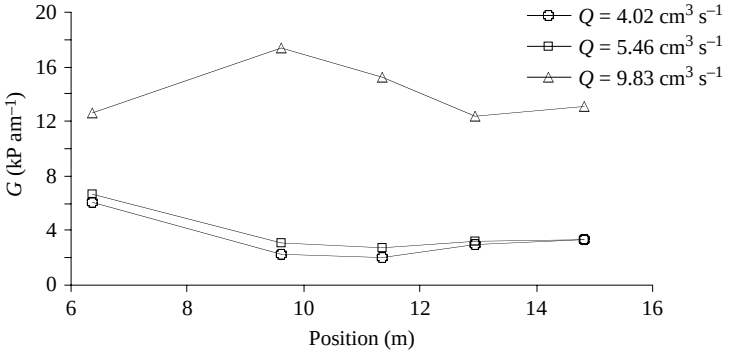

FIGURE 8. Pressure gradient measurements downstream of the static inline mixer.

(largest buoyancy number) follows the expected trend that indicates an approach towards fully developed flow. The intermediate flow rate also appears to be near the fully developed state at the end of the pipe. However, the highest flow rate (9.83 cm^3 s^{-1}) pressure gradient shows an interesting trend of increasing until a length of 10 m and then follows the trends displayed at the other flow rates. Since the pressure measurement at the first position in the flow system was near the limit of the Ashcroft test gauge, it is unclear if this is a real phenomena or a measurement error. However, the pressure gradient near the end of the flow loop indicates that the flow has most likely not travelled a sufficient distance to achieve a fully developed flow.

Norman *et al.* (2005) suggest that the length needed to obtain fully developed flow scales as

$$L_b = 0.12 \frac{R^3}{a^2 N_b} \frac{1}{f(\phi)}. \tag{6.1}$$

Although this correlation for the fully developed length scale considers only one particle type, it gives insight into the length needed to obtain fully developed flow in this bimodal suspension. Using the appropriate particle size and corresponding buoyancy number presented in table 2, a range of fully developed lengths can be determined from (6.1) for an equivalent suspension of a single particle type, shown in table 3.

Q (cm^3 s^{-1})	N_b(PMMA)	N_b(Ag)	L_{PMMA} (cm)	L_{Ag} (cm)
4.02	1.87	26.4	1000	2500
5.46	1.38	19.5	1300	3400
9.83	0.77	10.8	2400	6000

TABLE 3. Estimated fully developed length based on a single particle type at a bulk fraction of 0.30, where $L_b \sim 0.12[R^3/(a^2 N_b f(\phi))]$. L_{PMMA} is the estimated fully developed length for a system of PMMA particles. L_{Ag} is the fully developed length for a suspension of Ag particles.

The fully developed lengths in table 3 give lower and upper bounds for the fully developed length of the bimodal suspension. The Ag particles are much smaller in size and therefore require a significantly longer length to approach the fully developed state. However, comparing the values in table 3 with the pressure gradients in figure 8, it appears that the fully developed length is reached at some value between the predicted length for a suspension composed of PMMA particles and Ag particles. It is also clear from figure and the predicted lengths that highest flow rate (lowest buoyancy number) has not reached the fully developed state.

7. Experimental results

As shown in table 2 three flow rates, which correspond to six buoyancy numbers (three for each particle phase), were established and potential measurements were obtained at four sensor arrays for a frequency of 1 kHz (used to determine the average particle distribution) and 17.5 kHz (used to determine the particle distribution of the PMMA phase). The conductivity and the volume fraction of the two particle phases are related by Maxwell's equation,

$$\frac{\sigma}{\sigma_f} = 1 + 3\beta_{PMMA,f}\phi_{PMMA} + 3\beta_{Ag,f}\phi_{Ag}, \tag{7.1}$$

where σ is the conductivity of the suspension, σ_f is the conductivity of the suspending fluid, ϕ_{PMMA} is the volume fraction of PMMA particles and ϕ_{Ag} is the volume fraction of the Ag particles. The parameters $\beta_{PMMA,f}$ and $\beta_{Ag,f}$ are given by

$$\beta_{PMMA,f} = \frac{\sigma_{PMMA} - \sigma_f}{\sigma_{PMMA} + 2\sigma_f}, \qquad \beta_{Ag,f} = \frac{\sigma_{Ag} - \sigma_f}{\sigma_{Ag} + 2\sigma_f}. \tag{7.2a, b}$$

Here, σ_{PMMA} is the conductivity of the PMMA phase at a volume fraction ϕ_{PMMA} and σ_{Ag} is the conductivity of the Ag phase at a volume fraction of ϕ_{Ag}. The conductivity and volume fraction can be related with various correlations; however, in this study the Wagner correlation (Etuke 1994) is used,

$$\phi = \frac{\sigma_r - 1}{\sigma_r + 2}, \tag{7.3}$$

where $\sigma_r = \sigma_i/\sigma_f$. Since these correlations are valid for small volume fractions, a correction term is introduced to account for the larger volume fractions (see the Appendix).

By evaluating (7.1) at 1 kHz and 17.5k Hz, the volume fraction of both phases can be determined by using the measurements at the critical frequency to determine the volume fraction distribution of the PMMA particles. Once the conductivity profile of

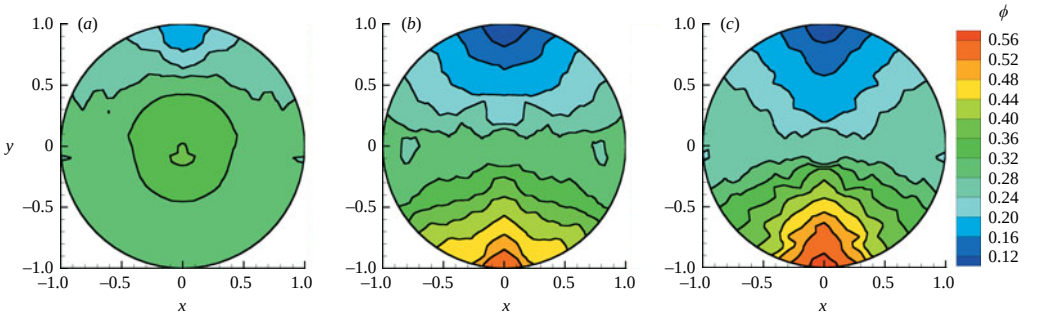

FIGURE 9. Bulk concentration profile for increasing buoyancy numbers at the last sensor, 13 m after the inline mixer. The average concentration, ϕ_{avg}, based on the integration of the contours is shown parenthetically. (*a*) $Q = 9.8\,\mathrm{cm^3\,s^{-1}}$ (0.296); (*b*) $Q = 5.5\,\mathrm{cm^3\,s^{-1}}$ (0.292); (*c*) $Q = 4.0\,\mathrm{cm^3\,s^{-1}}$ (0.286).

the PMMA phase is known, rearrangement of (7.1) results in a simple equation for the distribution of Ag particles.

7.1. *Total particle distribution*

The measurements at 1 kHz result in the concentration profile for the bulk particle phase and are used along with the measurements at 17.5 kHz to determine the concentration profile for each particle phase. Figure 9, for increasing buoyancy number, displays the total concentration profiles at the sensor furthest from the inline mixer (approximately 13 m).

The lowest flow rate (highest buoyancy number) bulk particle distribution shows the same trend as the single-particle-type suspension, with the particles accumulating at the bottom of the pipe. Additionally, these particle distributions show curvature due viscous resuspension. Further, the bimodal suspension shows larger accumulation of particles with larger magnitudes of buoyancy numbers.

At the highest flow rate, the particle distribution displays trends similar to neutrally buoyant particle suspensions, where particles accumulate at the low-shear zone near the centre of the pipe. This adverse density gradient of heavy fluid over light fluid was observed experimentally by Altobelli *et al.* (1991) for a system of heavy particles at a volume fraction of 0.39. A theoretical study by Zhang & Acrivos (1994) found similar results for a system similar to the experiments of Altobelli *et al.* More recently, Carpen & Brady (2002) performed a stability analysis for a gravity-driven flow through parallel plates. They determined that the wavelength with the maximum growth rate of this instability is on the order of the characteristic height of the flow system.

This adverse density gradient can be understood by considering the velocity scales of the flow. Specifically, the velocity of the settling particles can be expressed in terms of the corrected Stokes velocity

$$V_b = \frac{2(\rho_p - \rho_f)ga^2}{9\eta} f(\phi), \tag{7.4}$$

where V_b is the velocity due to buoyancy forces, ρ_i is the density of the particle or fluid phase, g is the gravitational constant, a is the radius of the particles, η is the viscosity and $f(\phi)$ is the hindered settling function. The velocity due to the shear-induced diffusion of the particles towards the low-shear zones opposes the velocity of the settling particles. The velocity due to shear-induced diffusion can be expressed in

N_b^c	13.83		
$N_b(\rho_{PMMA})$	0.77	1.38	1.87
$N_b(\rho_{Ag})$	10.8	19.5	26.4

TABLE 4. Prediction of unstable density gradient. The ratio of the shear-induced particle migration velocity to the velocity due to buoyancy forces. A ratio less than or equal to the critical buoyancy number (13.4 for this system) predicts an adverse density gradient.

terms of the radius of the pipe and the time scale for diffusion,

$$V_d = \frac{R}{t_d}, \tag{7.5}$$

where $t_d = R^2/4D$. Here, D is the hydrodynamic diffusion, which scales as the shear rate and is given by

$$D \sim \dot{\gamma} a^2 d(\phi). \tag{7.6}$$

A more useful expression is obtained by expressing the diffusion in terms of the average suspension velocity. The average shear rate for a pressure-driven pipe flow is

$$\dot{\gamma} \sim \frac{8U}{3R}. \tag{7.7}$$

Combining (7.5), (7.6) and (7.7) results in the following expression for the velocity of the particles due to shear-induced particle migration:

$$V_d = \frac{32}{3}\left(\frac{a}{R}\right)^2 U d(\phi). \tag{7.8}$$

When the shear-induced velocity exceeds the buoyancy-induced velocity, the adverse density gradient will occur. This can be expressed in the following ratio:

$$\frac{48U\eta d(\phi)}{(\rho_p - \rho_f) g R^2 f(\phi)} > 1, \tag{7.9}$$

which, in terms of the experimental buoyancy number, is

$$\frac{32 d(\phi)}{3 N_b f(\phi)} > 1. \tag{7.10}$$

A critical buoyancy number can be determine from (7.3) using the properties of this flow, where $d(\phi) \approx \phi^2$ (Nott & Brady 1994) and the hindered settling function is determined from (5.1) in § 5,

$$N_b^c = \frac{32 d(\phi)}{3 f(\phi)} = 13.83. \tag{7.11}$$

A flow with a buoyancy number less than this critical value can develop an adverse density gradient.

As shown in table 4 the lighter PMMA particles are predicted to develop an adverse density gradient, along with the lowest buoyancy number for the Ag phase. As will be seen, two of the flow rates for the PMMA phase and the lowest flow rate for the Ag phase displayed adverse density gradients, which will be discussed further in the following sections.

7.2. *PMMA and Ag particle phases*

The PMMA particle phase is determined directly from the measurements at 17.5 kHz. The signal-to-noise ratio starts to decrease rapidly around 15 kHz. This resulted in data sets that contained more noise than the data obtained at 1 kHz. To compensate for this, the potential measurements obtained at 17.5 kHz were inverted using a coarser grid. Specifically, several elements of the finite element grid were assigned constant conductivity values, which resulted in 72 conductivity zones.

Figure 10 shows the particle distribution for the PMMA and the Ag particles at the last sensor downstream of the inline mixer, for decreasing buoyancy number. The accumulation of particles for each phase is seen to increase as the magnitude of the buoyancy number increases. Furthermore, the data for the lowest buoyancy number reveal that the adverse density gradient still persists. However, it should be noted that this flow rate has not reached the fully developed state.

7.3. *Developing particle phases*

The developing particle phases along the flow system are described in this section. The data are presented for increasing length downstream of the inline mixer. The PMMA particle phase was obtained from the potential measurement obtained at 17.5 kHz and the Ag particle phases are obtained using the procedure discussed at the start of this section. The data obtained at 17.5 kHz is at the limit of the performance of the inline sensors. Therefore, some of the potential measurement data were contaminated with higher levels of noise, which prevented their inversion. However, much was of a sufficient quality to enable inversion. The position where the data were obtained is indicated in the figure captions.

Figure 11 shows the development of the PMMA and Ag particle phase for the lowest flow rate. There is increasing particle deposition as the suspension proceeds to the fully developed state. Both particle phases show deposition early in the flow system and there is no sign of an adverse density gradient for this flow rate.

Figure 12 shows the development of the particle phase for the intermediate flow rate of $Q = 5.46\,\mathrm{cm^3\,s^{-1}}$. An adverse density gradient is apparent in the early stages of the flow for the PMMA particle phase. However, as the suspension approaches the fully developed state, the PMMA phase settles to a stable density profile with the lighter fluid over the heavier fluid.

Figure 13 shows the development for the highest flow rate of $Q = 9.83\,\mathrm{cm^3\,s^{-1}}$. The data for this flow rate contained a higher level of noise, and therefore, only two sensor arrays provided data that were sufficiently low in noise to determine the concentration profile. The concentration profiles are presented for the inline sensors furthest downstream of the inline sensors. As seen in this figure, both phases reveal an adverse density gradient. However, as discussed previously, this flow rate has not travelled a sufficient distance to reach the fully developed state, and it appears as if the unstable density gradient is transitioning towards a stable orientation as seen in the intermediate flow rate.

7.4. *Comparison to single particle suspensions*

Figure 14 compares the results for a similar system of single-particle-type suspensions obtained by Norman *et al.* (2004) and the Ag particle phase of the bimodal suspension. The single-particle system consists of 20 % by volume of Ag particles, whereas the Ag particle phase in the bimodal suspension consists of 15 % by volume particles. Although the composition differs slightly, a comparison of these two suspensions at

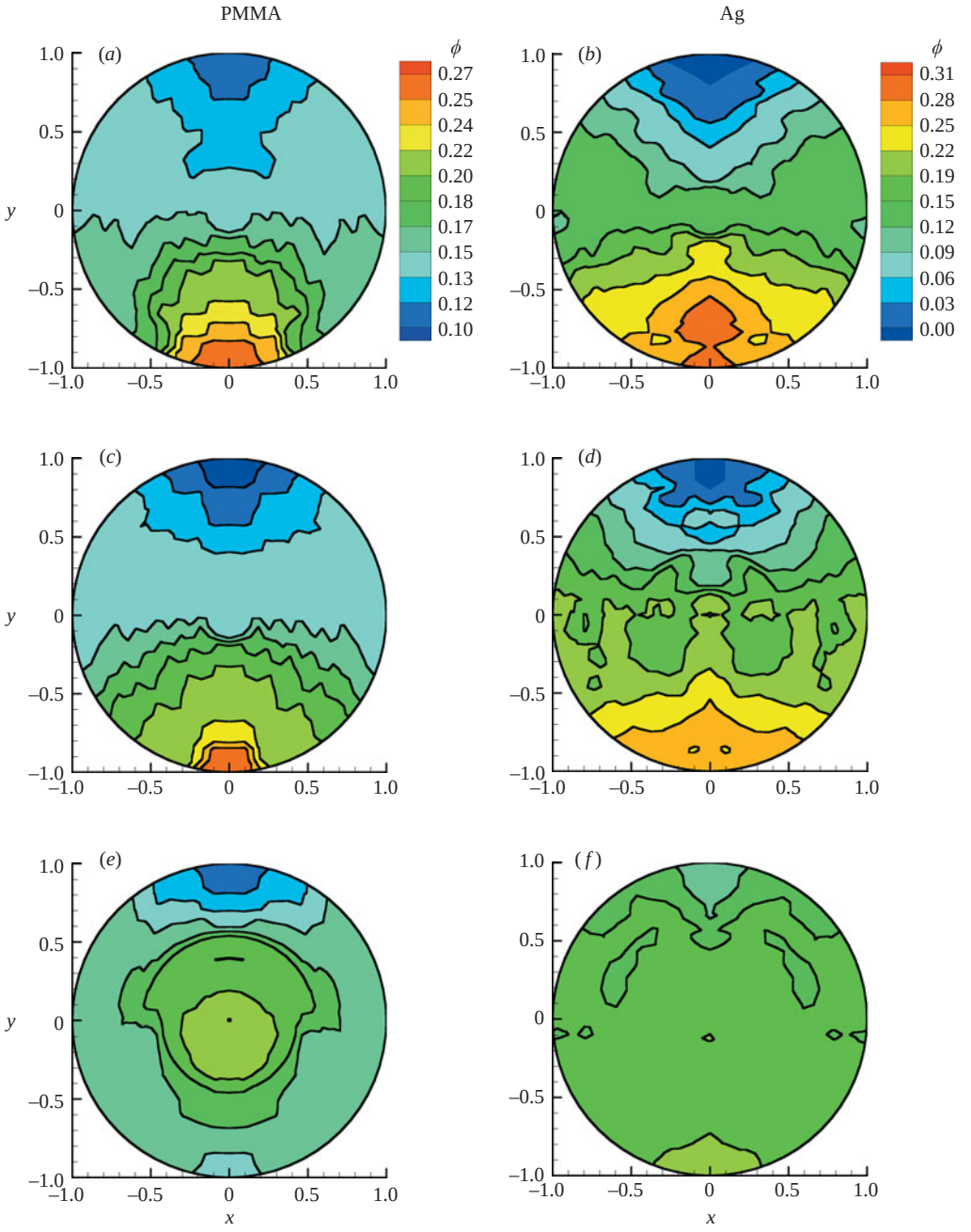

FIGURE 10. Concentration profile for the PMMA (left column) and Ag (right column) particle phases at the last sensor downstream of the inline mixer. The average concentration, ϕ_{avg}, based on the integration of the contours is shown parenthetically. (*a*) $N_b = 1.87$ (0.160); (*b*) $N_b = 26.4$ (0.150); (*c*) $N_b = 1.38$ (0.159); (*d*) $N_b = 19.5$ (0.162); (*e*) $N_b = 0.77$ (0.170); (*f*) $N_b = 10.8$ (0.163).

similar buoyancy numbers and near the fully developed state (the data are obtained at the last sensor in the flow system) will give insight into the behaviour of the suspension when two particle types are present.

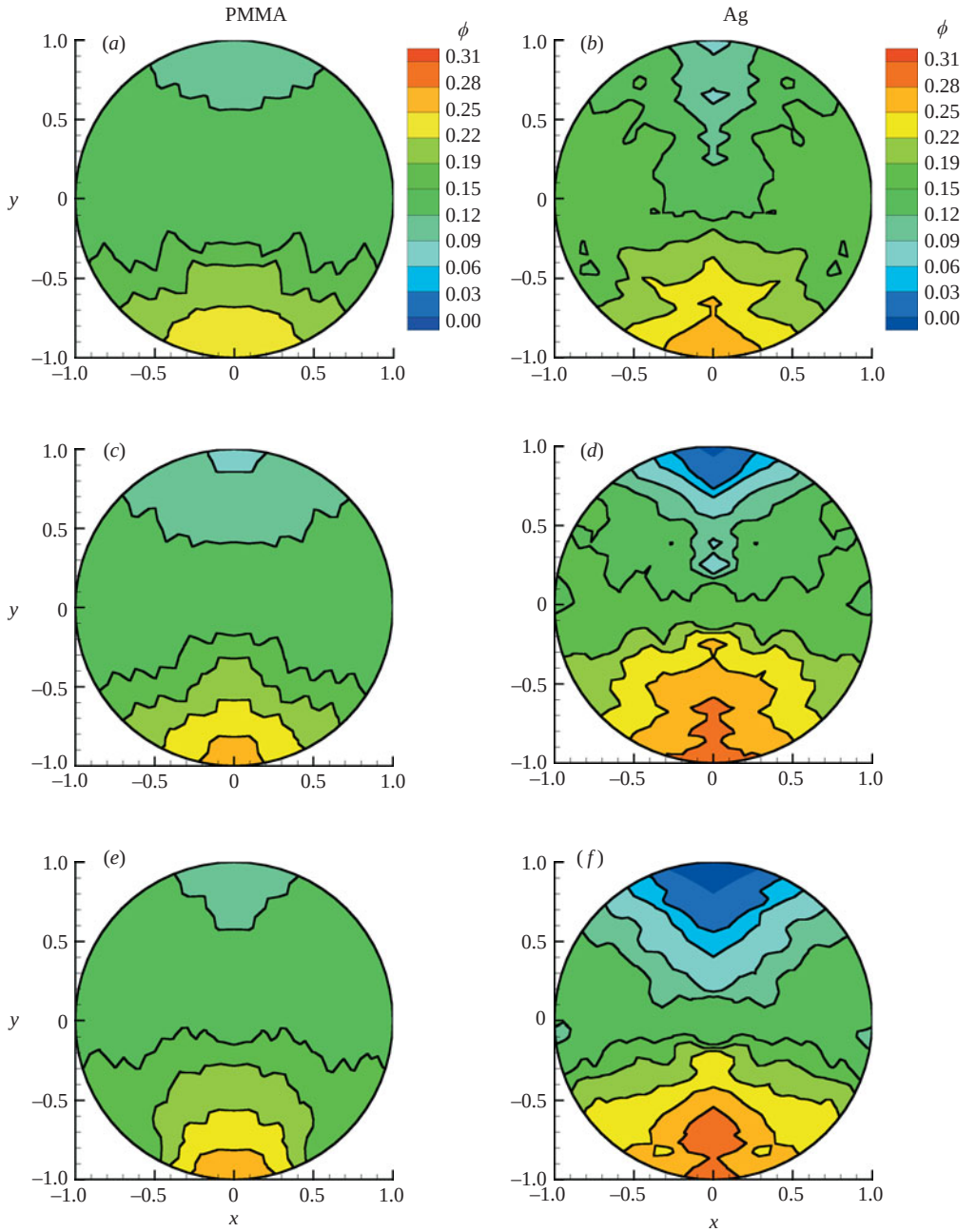

FIGURE 11. Developing concentration profile for the lowest flow rate $Q = 4.02\,\mathrm{cm}^3\,\mathrm{s}^{-1}$. The left column presents the PMMA particle phase and the right column presents the Ag particle phase. The average concentration, ϕ_{avg}, based on the integration of the contours is shown parenthetically. Data were obtained at locations: (*a*) 5.5 m (0.154); (*b*) 5.5 m (0.168); (*c*) 11.4 m (0.151); (*d*) 11.4 m (0.172); (*e*) 13.0 m (0.160); (*f*) 13.0 m (0.150).

As seen in figure 14, the deposition of the particles in the bimodal suspension is significantly diminished. The primary reason for the decreased deposition is the increased interaction of the particles at this concentration resulting in a more

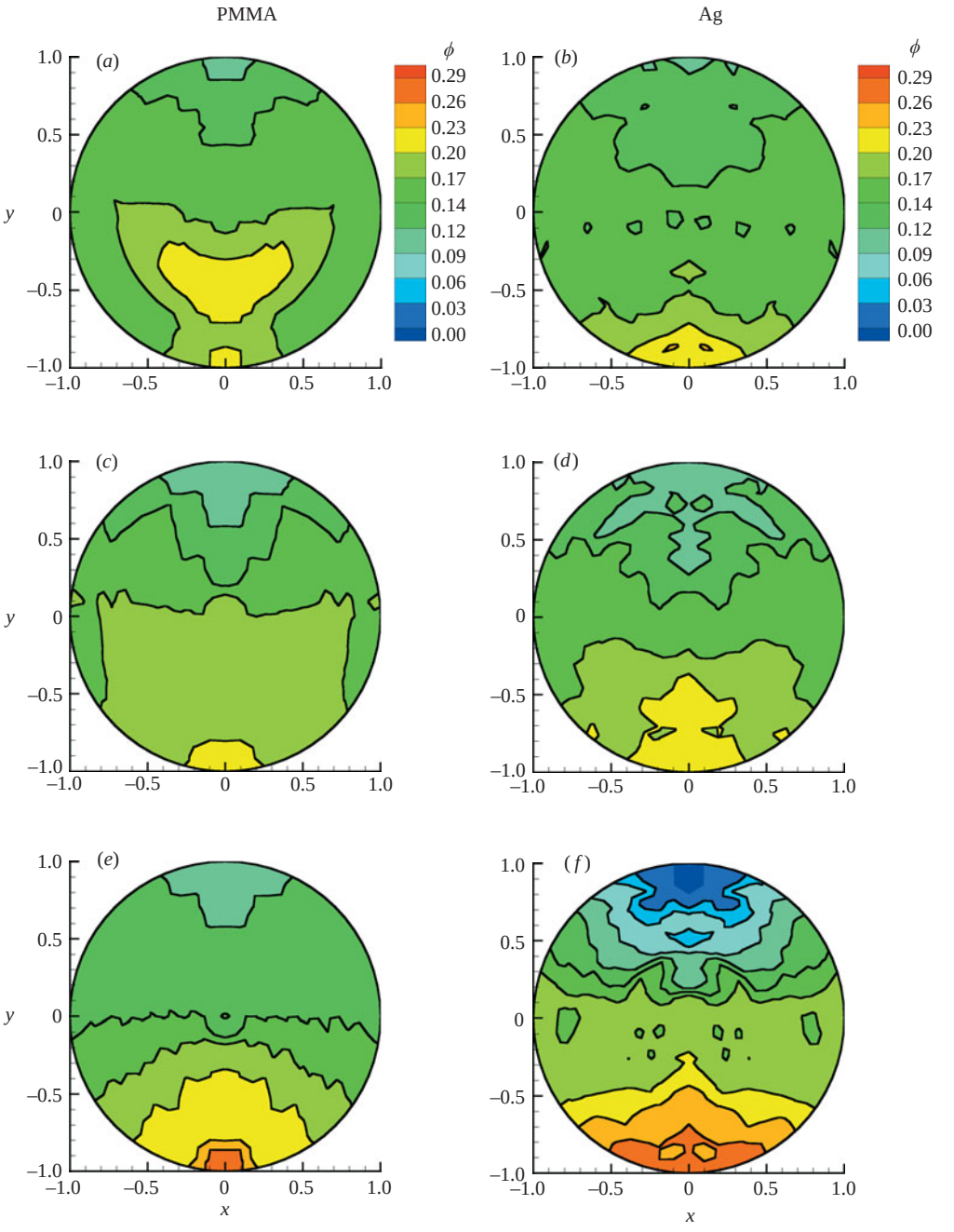

FIGURE 12. As figure 11 but for the intermediate flow rate $Q = 5.46\,\mathrm{cm^3 s^{-1}}$. The average (*a*) 5.5 m (0.169); (*b*) 5.5 m (0.157); (*c*) 10.0 m (0.169); (*d*) 10.0 m (0.161); (*e*) 13.0 m (0.159); (*f*) 13.0 m (0.162).

significant diffusion towards the low-shear zones. Additionally, the particles settle less rapidly as the bulk concentration increases.

To quantify the experimental results presented above, a moment analysis is used. One moment, or integral, of the concentration fields is defined to represent the vertical

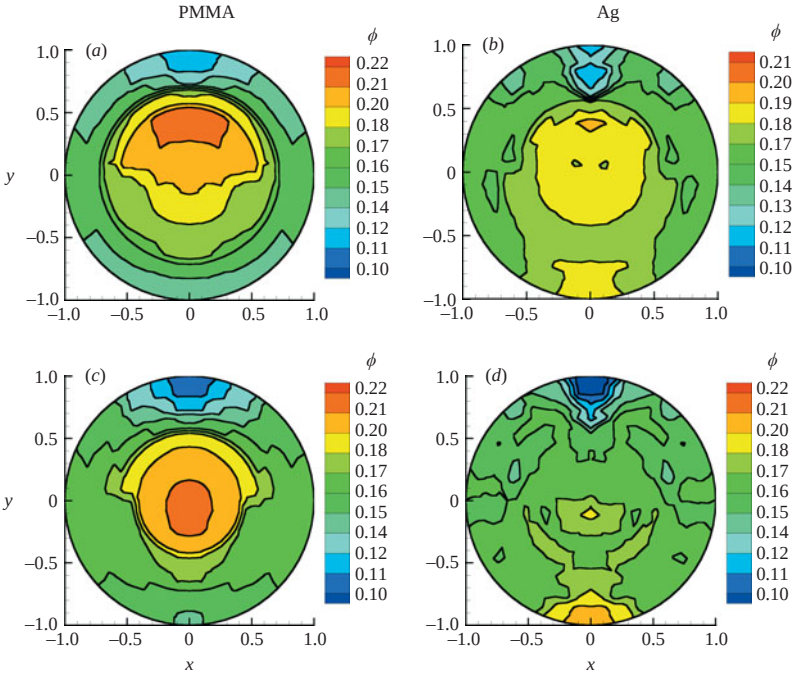

FIGURE 13. As figure 11 but for the highest flow rate $Q = 9.83\,\mathrm{cm}^3\,\mathrm{s}^{-1}$. (*a*) 11.4 m (0.170); (*b*) 11.4 m (0.166); (*c*) 13.0 m (0.170); (*d*) 13.0 m (0.163).

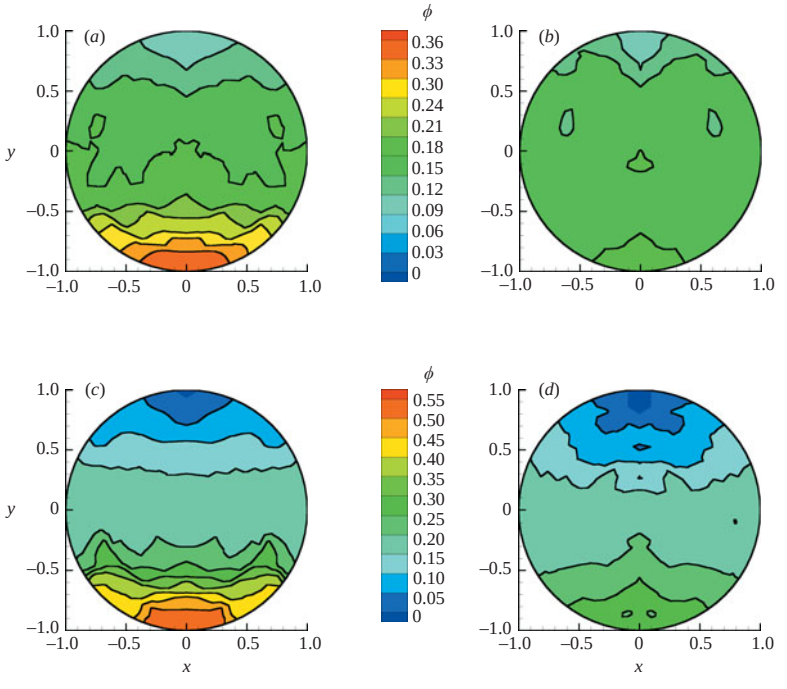

FIGURE 14. Comparison of single-particle-type suspension and the Ag phase of the bimodal particle system. The left column shows the single-particle system composed of 20 % by volume of Ag particles and the right column show the Ag phase of the bimodal suspension, which consists of 15 % by volume of particles. (*a*) $N_b = 9.5$; (*b*) $N_b = 10.8$; (*c*) $N_b = 18.6$; (*d*) $N_b = 19.5$.

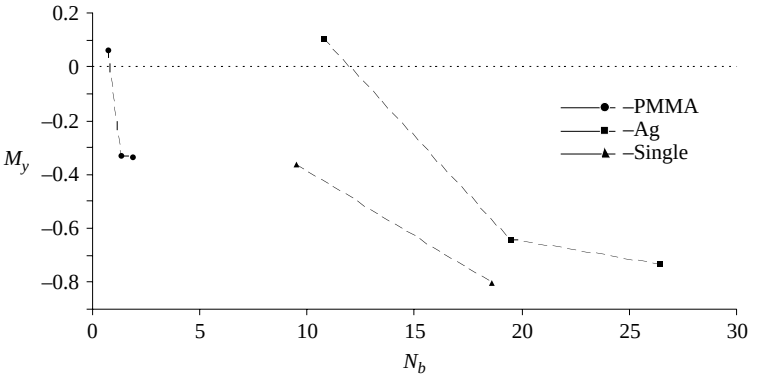

FIGURE 15. Moment for the bimodal suspension phases. The circular symbols represents the PMMA particle phase and the square symbols represent the Ag particle phase. The triangular symbols represent the moments for the single particle-type suspension at similar conditions obtained from the study by Norman, Nayak & Bonnecaze (2004).

distribution of particles at the sensor array furthest downstream of the inline mixer. The moment (M_y) represents the vertical distribution as is given by

$$M_y \equiv \frac{1}{\phi_b} \int_A \phi(x, y) y \, \mathrm{d}A. \tag{7.12}$$

Here, ϕ_b is the bulk volume fraction, which is 0.15 for both the lighter (PMMA) particle and the heavier (Ag) particle suspensions. Further, the sign of this moment represents the distribution of the particles, where a negative sign indicates that a larger fraction of the particles is near the bottom of the pipe and a positive sign indicates that a larger fraction of the particles is above the centreline.

Figure 15 shows the moment for the two particle phases. The data are for the sensor furthest downstream of the inline mixer. To quantify the difference in the particle distribution for a single-particle-type suspension and a bimodal suspension, the moment for similar single-particle-type suspensions obtained by Norman *et al.* (2004) is also included in figure 15. This figure clearly reveals a larger deposition of particles for the single-particle suspension, and further exemplifies the hindering effect of the lighter PMMA particles and the increased shear-induced particle migration to the low-shear zones at the higher concentrations in the bimodal suspension.

7.5. *Comparison to suspension balance model*

One of the reasons this research was undertaken is to determine if the predictions by a suspension balance model match qualitatively and quantitatively the experimental data obtained from EIT imaging. The experimental results are therefore compared to the numerical results; specifically the experimental result at 17.5 kHz (PMMA) and the results from the suspension balance model for the PMMA phase are compared. Further comparison is made between the experimental result at 1 kHz and the total concentration distribution profile obtained from the suspension balance model.

Figure 16 represents the experimental volume fraction of PMMA compared to the prediction of the suspension balance model. All the experimental profiles match the numerical predictions of the suspension balance model qualitatively. In addition, there is an excellent match between the experimental concentrations and predicted values within the depletion and accumulation zones at the top and bottom of the pipe

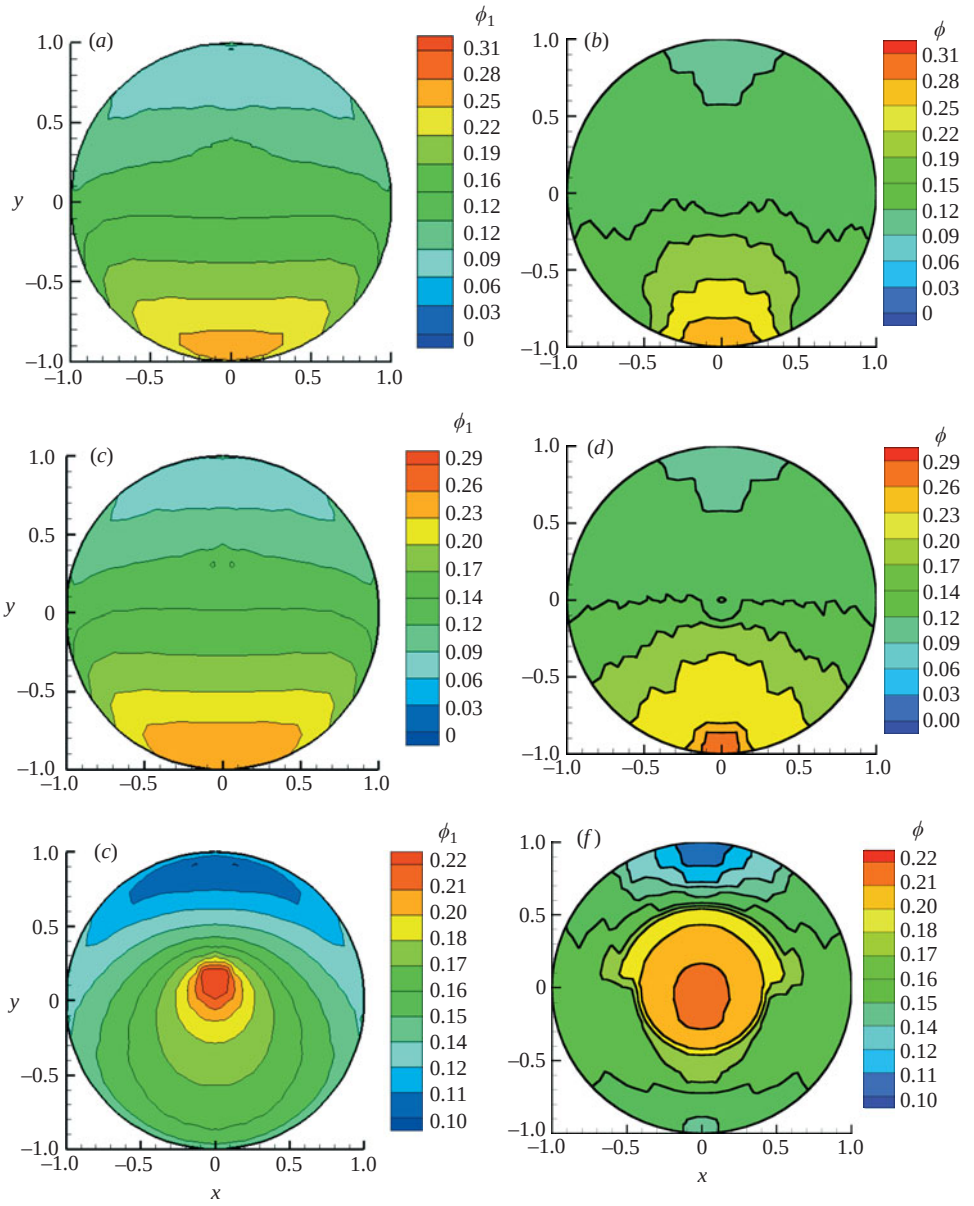

FIGURE 16. Comparison of theoretical (left-hand column) and experimental results (right-hand column) for the PMMA particle phase. The experimentally obtained concentration profiles are taken 13 m after the inline mixer. The theoretical results were obtained using the suspension balance model. The data are presented for all the flow rates. (a, b) $Q = 4.02\,\mathrm{cm^3\,s^{-1}}$; (c, d) $Q = 5.46\,\mathrm{cm^3\,s^{-1}}$; (e, f) $Q = 9.86\,\mathrm{cm^3\,s^{-1}}$.

respectively. The large discrepancy noticed between the theoretical and experimental profiles at the centre of the pipe in the monodisperse case by Norman *et al.* (2005) is clearly absent in this bimodal study.

While the magnitudes of the concentrations predicted by theory and experiment are correct over regions of the pipe, the shapes of the theoretical iso-concentration

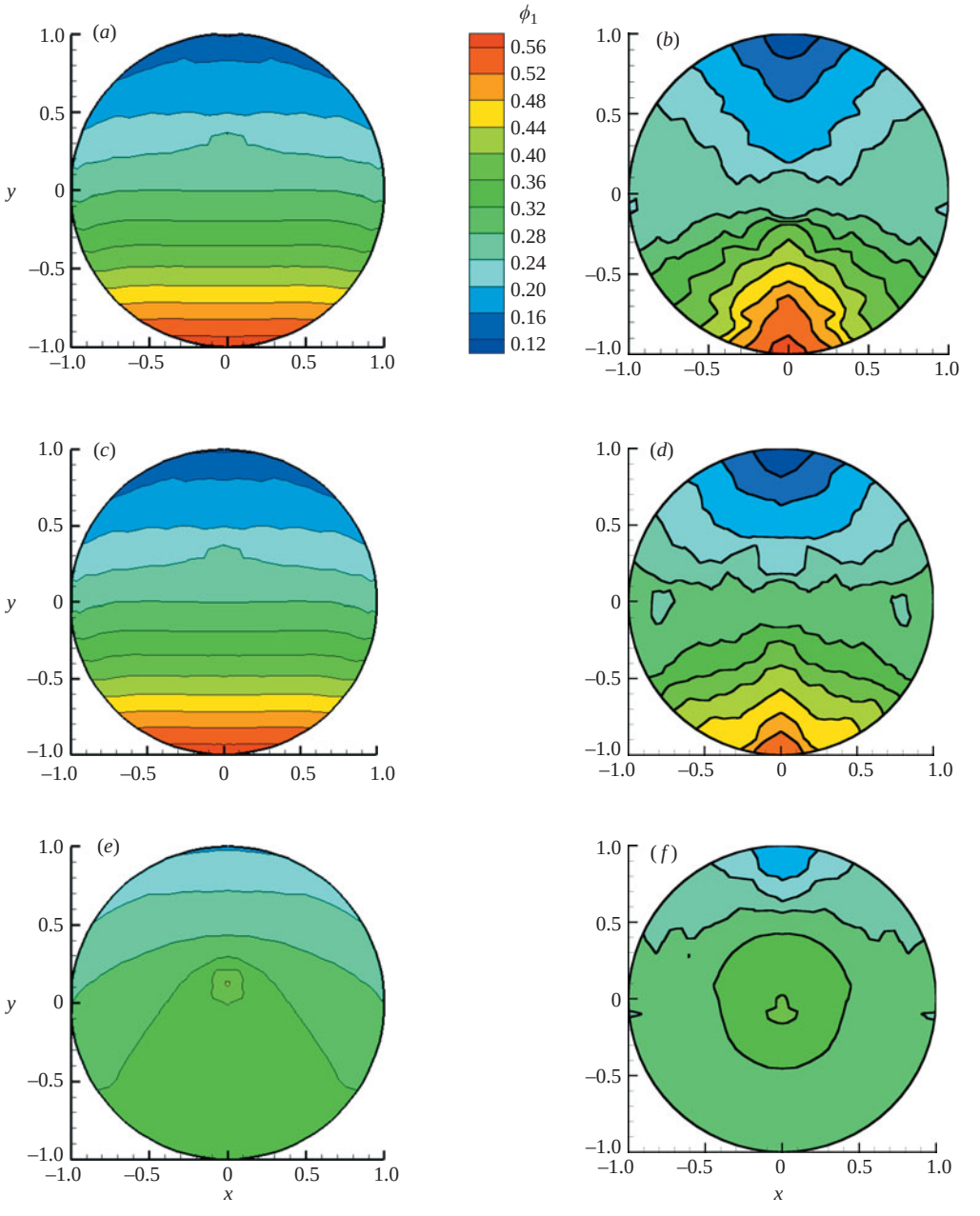

FIGURE 17. Comparison of theoretical (left-hand column) and experimental results (right-hand column) for the suspension. The experimentally obtained concentration profiles are at 13 m after the inline mixer. The theoretical results were obtained using the suspension balance model. The data are presented for all the flowrates. (*a*) $Q = 4.02\,\mathrm{cm^3\,s^{-1}}$, theoretical; (*b*) $Q = 4.02\,\mathrm{cm^3\,s^{-1}}$, experimental; (*c*) $Q = 5.46\,\mathrm{cm^3\,s^{-1}}$, theoretical; (*a*) $Q = 5.46\,\mathrm{cm^3\,s^{-1}}$, experimental; (*b*) $Q = 9.86\,\mathrm{cm^3\,s^{-1}}$, theoretical; (*c*) $Q = 9.86\,\mathrm{cm^3\,s^{-1}}$, experimental.

lines are not in agreement with those observed experimentally. The model employed here assumes that the normal stresses due to the suspension are isotropic. In-plane velocities, though weak (Norman *et al.* 2005), could be sensitive to this assumption

and alter the 'tilt' of the iso-concentration lines. A model of the form proposed by Morris & Boulay (1999) or Fang *et al.* (2002) may account for these discrepancies.

Figure 16(f) shows some interesting trends. The experiment was performed at a relatively high flow rate, hence a low buoyancy number, and the concentration profile may not represent the fully developed flow. The large concentration of PMMA particles around the centre implies this, but more interesting is the fact that the adverse density gradient in the centre was sufficiently resolved by the sensors. The predicted concentration profile, figure 16(e) shows a smaller adverse density gradient which corroborates the fact that the trend noticed in Figure 16(f) may be transitioning towards a more stable state. The fact that the sensors were able to resolve the conductivity differences at the centre for this relatively large flow rate casts some doubts on the argument by Norman (2004) that discrepancies between experimental and theoretical profiles observed at the centre for the first two flow rates may be due to imaging errors. The profile of the total concentration (figure 17) shows similar trends to those exhibited by the PMMA particle phase discussed above.

8. Conclusions

We have used a non-invasive imaging technique to study particle migration in a bimodal suspension of 15 % by volume of buoyant PMMA particles and 15 % by volume of buoyant Ag particles. The resulting concentration profiles reveal an unstable density gradient, which appears to transition to a stable density profile as the suspension approaches the fully developed state. This adverse density gradient is more apparent for the lighter PMMA particle phase and the highest flow rate shows persistence of this adverse gradient. However, it must be noted that this flow rate has not reached the fully developed state, and the intermediate flow rate shows that this adverse density gradient returns to a stable configuration at the fully developed state. Further, the concentration profiles obtained using ERT show that the deposition of particles is hindered by the presence of the additional particle phase.

It was also shown that the scaling argument for the fully developed length of buoyant suspensions at low Reynolds numbers presented by Norman *et al.* (2005) gives the upper and lower limits for the fully developed state of a bimodal suspension. Furthermore, the developing pressure gradient resembles that of a single-particle-type suspension, where the pressure gradient drops initially and then increases to a larger fully developed value.

The theoretical predications of the suspension balance model qualitatively match the experimental observations very well. Further, there is fair quantitative agreement between the predictions and the observations of the phase distributions of each type of particle. This is gratifying considering that the assumption of the partial pressures of the particle phase following an ideal mixing relationship is *ad hoc*.

In summary, ERT images have provided valuable insight into the behaviour of low-Reynolds-number suspension flows when two types of buoyant particle are present and the suspension balance model captures the essential features of the distribution of each particle phase.

Appendix

Suspensions consisting of a single particle type (with the same suspending fluid as the experiments) were mixed uniformly at various concentrations. At each concentration the uniform conductivity was determined using the sensor arrays and

inverse algorithm described in Norman (2004). These data provide the information necessary to determine a correction factor for the conductivity in (5.3). For the PMMA suspension at 17.5 kHz, the corrected conductivity is

$$\bar{\sigma}_{PMMA}(17.5kHz) = \sigma_{PMMA}\big(403162\sigma_{PMMA}^5 - 198485\sigma_{PMMA}^4 + 36375\sigma_{PMMA}^3 - 2965.4\sigma_{PMMA}^2 + 92.713\sigma_{PMMA} + 0.9102\big). \quad \text{(A 1)}$$

Here, $\bar{\sigma}_{PMMA}$ is the corrected conductivity and σ_{PMMA} is the conductivity determined with the inverse algorithm. Using the same procedure, the conductivity of a PMMA suspension at 1 kHz is corrected by

$$\bar{\sigma}_{PMMA}(1kHz) = \sigma_{PMMA}\big(-8377.3\sigma_{PMMA}^4 + 3725.2\sigma_{PMMA}^3 - 554.77\sigma_{PMMA}^2 + 28.106\sigma_{PMMA} + 0.9722\big). \quad \text{(A 2)}$$

The conductivity of the Ag suspension is corrected at 1 kHz by

$$\bar{\sigma}_{Ag}(1kHz) = \sigma_{Ag}\big(2379.9\sigma_{Ag}^3 - 996.85\sigma_{Ag}^2 + 135.39\sigma_{Ag} - 4.9282\big). \quad \text{(A 3)}$$

REFERENCES

Altobelli, S. A., Givler, R. C. & Fukushima, E. 1991 Velocity and concentration measurements of suspensions by nuclear magnetic resonance imaging. *J. Rheol.* **35**, 721–734.

Altobelli, S. A. & Mondy, L. A. 2002 Hindered flotation functions from nuclear magnetic resonance imaging. *J. Rheol.* **46**, 1341–1352.

Beyea, S. D., Altobelli, S. A. & Mondy, L. A. 2003 Chemically selective NMR imaging of a 3-component (solid-solid-liquid) sedimenting system. *J. Magnetic Resonance* **161**, 198–203.

Butler, J. E. 1998 Tomographic imaging for the visualization of multiphase flows. PhD thesis, The University of Texas at Austin.

Butler, J. E. & Bonnecaze, R. T. 1999 Imaging of particle shear migration with electrical impedance tomography. *Phys. Fluids* **11**, 1982.

Butler, J. E., Majors, P. D. & Bonnecaze, R. T. 1999 Observations of shear-induced particle migration for oscillatory flow of a suspension within a tube. *Phys. Fluids* **11**, 2865–2877.

Carpen, I. C. & Brady, J. F. 2002 Gravitational instability in suspension flow. *J. Fluid Mech.* **472**, 201–210.

Chang, C. & Powell, R. L. 1993 Dynamic simulation of bimodal suspensions of hydrodynamically interacting spherical particles. *J. Fluid Mech.* **253**, 1–25.

Chang, C. & Powell, R. L. 1994 Self-diffusion of bimodal suspensions of hydrodynamically interacting spherical particles in shear flow. *J. Fluid Mech.* **281**, 51–80.

Chorin, A. J. 1967 A numerical method for solving incompressible viscous flow problems. *J. Comput. Phys.* **135**, 118–125.

Chow, A. W., Sinton, S. W., Iwaniya, J. H. & Stephens, T. S. 1994 Shear-induced migration in Couette and parallel-plate viscometers: NMR imaging and stress measurements. *Phys. Fluids* **8**, 2561–2576.

Dickin, F. & Wang, M. 1996 Electrical resistance tomography for process applications. *Meas. Sci. Technol.* **7**, 247–260.

Etuke, E. O. 1994 Impedance spectroscopy for component specificity in tomographic imaging. PhD thesis, University of Manchester Institute of Science and Technology.

Fang, Z., Mammoli, A. A., Brady, J. F., Ingber, M. S., Mondy, L. A. & Graham, A. L. 2002 Flow-aligned tensor models for suspension flows. *Intl J. Multiphase Flow* **28**, 137–166.

Gadala-Maria, F. & Acrivos, A. 1980 Shear-induced structure in a concentrated suspension of solid spheres. *J. Rheol.* **24**, 799–814.

Hampton, R. E., Mammoli, A. A., Graham, A. L. & Tetlow, N. 1997 Migration of particles undergoing pressure-driven flow in a circular conduit. *J. Rheol.* **41**, 621–640.

Husband, D. M., Mondy, L. A., Ganani, E. & Graham, A. L. 1994 Direct measurements of shear-induced particle migration in suspensions of bimodal spheres. *Rheol. Acta.* **33**, 185–192.

Koh, C. J., Hookham, P. & Leal, L. G. 1994 An experimental investigation of concentrated suspension flows in a rectangular channel. *J. Fluid Mech.* **266**, 1–32.

Leighton, D. & Acrivos, A. 1987 The shear-induced migration of particles in concentrated suspension. *J. Fluid Mech.* **181**, 414–439.

Lenoble, M., Snabre, P. & Pouligny, B. 2005 The flow of a very concentrated slurry in a parallel-plate device: Influence of gravity. *Phys. Fluids* **17**, 073303.

Lyon, M. K. & Leal, L. G. 1998*a* An experimental study of the motion of concentrated suspensions in two-dimensional channel flow. Part 1. Monodisperse systems. *J. Fluid Mech.* **363**, 25–56.

Lyon, M. K. & Leal, L. G. 1998*b* An experimental study of the motion of concentrated suspensions in two-dimensional channel flow. Part 2. Bidisperse systems. *J. Fluid Mech.* **363**, 57–77.

Miller, R. M. & Morris, J. F. 2006 Normal stress-driven migration and axial development in pressure-driven flow of concentrated suspensions. *J. Non-Newtonian Fluid Mech.* **135**, 149–165.

Morris, J. F. & Boulay, F. 1999 Curvilinear flows of noncollodial suspensions: the role of normal stresses. *J. Rheol.* **43**, 1213–1237.

Norman, J. T. 2004 Imaging particle migration with electrical impedance tomography: an investigation into the behaviour and modelling of suspension flows. PhD thesis, The University of Texas at Austin.

Norman, J. T & Bonnecaze, R. T. 2005 Measurement of solids distribution in suspension flows using electrical resistance tomography. *Can. J. Chem. Engng* **83**, 24–36.

Norman, J. T., Nayak, H. V. & Bonnecaze, R. T. 2005 Migration of buoyant particles in low Reynolds number, pressure-driven flows. *J. Fluid Mech.* **523**, 1–35.

Nott, P. R. & Brady, J. F. 1994 Pressure-driven flow of suspensions: simulation and theory. *J. Fluid Mech.* **275**, 157–199.

Parker, L. R. 1994 *Geophysical Inverse Theory*. Princeton University Press.

Phillips, R. J., Armstrong, R. C., Brown, R. A., Graham, A. L. & Abbott, J. R. 1992 A constitutive equation for concentrated suspensions that accounts for shear-induced particle migration. *Phys. Fluids* A **4**, 30–40.

Shauly, A., Wachs, A. & Nir, A. 1998 Shear-induced particle migration in a polydisperse concentrated suspension. *J. Rheol.* **42**, 1329–1348.

Shapiro, A. P. & Probstein, R. F. 1992 Random packings of spheres and fluidity limits of monodisperse and bidisperse suspensions. *Phys. Rev. Lett.* **68**, 1422–1425.

Storms, R. F., Ramaro, B. V. & Weiland, R. H. 1990 Low shear rate viscosity of bimodally dispersed suspensions. *Powder Tech.* **63**, 247–259.

Tetlow, N. & Graham, A. L. 1998 Particle migration in a Couette apparatus; Experiment and modeling. *J. Rheol.* **42**, 307–327.

Tripathi, A. & Acrivos, A. 1999 Viscous resuspension in a bidensity suspension. *Intl J. Multiphase Flow* **25**, 1.

Zhang, K. & Acrivos, A. 1994 Viscous resuspension in fully developed laminar pipe flow. *Intl J. Multiphase Flow* **20**, 579–591.